Revision 2

Synthesis of quenchable high-pressure form of magnetite (h-Fe_3O_4) with composition $^{Fe1}(Fe^{2+}_{0.75}\ Mg_{0.26})\ ^{Fe2}(Fe^{3+}_{0.70}\ Cr_{0.15}Al_{0.11}\ Si_{0.04})_2O_4$

Monika Koch-Müller[1], Enrico Mugnaioli[2,3], Dieter Rhede[4], Sergio Speziale[1], Ute Kolb[2, 5], Richard Wirth[1]

[1] Sektion 3.3, Chemie und Physik der Geomaterialien, Deutsches GeoForschungsZentrum, Telegrafenberg, 14473 Potsdam, Germany

[2] Institut für Physikalische Chemie, Johannes Gutenberg-Universität, Jakob-Welder-Weg 11, 55128 Mainz, Germany

[3] University of Siena, Department of Physical, Earth and Environmental Sciences, Via Laterina 8 53100 Siena, Italy

[4] Sektion 4.2, Anorganische und Isotopenchemie, Deutsches GeoForschungsZentrum, Telegrafenberg, 14473 Potsdam, Germany

[5] Institute für Angewandte Geowissenschaften, Technische Universität Darmstadt, Schnittspahnstr. 9, 64287 Darmstadt, Germay.

keywords: Fe-oxide, h-Fe_3O_4, high-pressure, electron transmission microscopy, electron diffraction tomography, electron energy loss spectroscopy, electron microprobe analyses, crystal chemistry

Abstract

We report the synthesis of h-magnetite, ideally h-Fe_3O_4 with considerable amounts of substitutional cations (Cr, Mg, Al, Si) and quenchable to ambient conditions. Two types of experiments were performed at 18 GPa and 1800 °C in a multi-anvil press. In one we used an oxide mixture with a majoritic stoichiometry $Mg_{1.8}Fe_{1.2}(Al_{1.4}\ Cr_{0.2}Si_{0.2}Mg_{0.2})Si_3O_{12}$, with Si and Mg in excess as starting material (MA-367, MA-380). In the second type of experiment (MA-376) we started from an oxide mixture on the composition of the Fe-oxide phase obtained in MA-367. The Fe-oxide phases of both experiments were investigated by electron microprobe, transmission electron microscopy including electron diffraction tomography. Our investigations show that the Fe-oxide phases crystallize in the structure-type of h-magnetite. However, electron diffraction data show that keeping the cell setting from literature, this phase crystallizes in space group *Amam* and not in space group *Bbmm* as previously proposed. In the experiment MA-367 the Fe-oxide phase are mutually intergrown with majorite, the major phase of the run products. The formula for h-magnetite in this run was calculated as $^{Fe1}(Fe^{2+}_{0.75}\ Mg_{0.26})\ ^{Fe2}(Fe^{3+}_{0.70}\ Cr_{0.15}Al_{0.11}\ Si_{0.04})_2O_4$. In the experiment on the bulk composition of the Fe-oxide the main phase was h-magnetite with composition $^{Fe1}(Fe^{2+}_{1.02})\ ^{Fe2}(Fe^{3+}_{0.65}\ Cr_{0.19}Al_{0.13}\ Si_{0.03})_2O_4$ and traces of nearly pure end-member wadsleyite and stishovite. Our results indicate that the substitution of 20 to 30% of Fe (0.7 to 0.9 atoms per formula unit) by smaller cations favored the preservation of the high-pressure form to ambient conditions. We prove that the h-magnetite-type oxide is also stable in chemical systems more complex than Fe-O. Based on our results obtained at 18 GPa and 1800 ºC in a system (MA-367) that is closely related to Fe-enriched oceanic lithospheric material, we suggest that a Fe_3O_4-rich phase may be present in environments connected to deeply subducted slabs, and possibly associated with deep carbonatitic melting. Our observations show that Cr strongly

partitions in the oxide phase such that the coexisting silicates are depleted in Cr compared to Fe_3O_4-free assemblages. This may significantly affect the chemical signature of melts produced in the deep mantle.

Introduction

The discovery of the high-pressure Fe-oxide Fe_4O_5 (Lavina et al. 2011) revealed that the Fe-oxide phase relations, especially at high pressures, are still poorly understood. Under ambient conditions, the Fe-oxides FeO (wüstite), Fe_3O_4 (magnetite), and Fe_2O_3 (hematite) are stable and form complex defect structures. Stoichiometric FeO is very difficult to synthesize – wüstite chemical composition is more realistically written as $Fe_{1-x}O$ (Hazen and Jeanloz, 1984). It crystallizes in the cubic NaCl-type structure and forms a solid solution series with MgO (periclase). Magnetite is a cubic inverse-spinel-type ferrite whose unit cell contains eight Fe^{3+} in the tetrahedral sites, and a "uniform", mixed-valence occupancy of eight Fe^{2+} plus eight Fe^{3+} in the octahedral sites. Common impurities in natural magnetite are traces of Mg, Zn, Mn, Ni, Cr, Ti, V (Bowles et al. 2011). Fe_2O_3 occurs in different modifications, with hematite (α-Fe_2O_3) as the most prominent one. Hematite is known to incorporate traces of Ti, Al, and Mn (Bowles et al. 2011).

All three Fe-oxides show non-quenchable, pressure-induced phase transitions. According to Ono et al. (2004) hematite transforms at 30 GPa and 1800–2200° C into a perovskite-type structure. Wüstite at ambient temperature transforms at pressure above 17 GPa into a rhombohedral or monoclinic polymorph (Zou et al. 1980; Shu et al. 1998; Fei et al. 1996; Kantor et al., 2008; Fisher et al. 2011) and to a NiAs-type polymorph at pressures above 60 GPa and high temperatures (e.g. Fei and Mao, 1994; Kondo et al., 2004).

The phase diagram of Fe_3O_4 is still controversal: According to Pasternak et al. (1994) cubic inverse-spinel magnetite transforms at $P > 25$ GPa and room temperature to a monoclinic

high pressure phase. Dubrovinsky et al. (2003) and Lazor et al. (2007) propose $P > 19$ GPa as pressure for the transition of magnetite to h-magnetite at room temperature. In a Mössbauer and X-ray diffraction study Rozenberg et al. (2007) reported a pressure-induced transformation of inverse magnetite to normal-spinel magnetite at 8 GPa. However, Glazyrin et al. (2012) did not observe for magnetite the inverse to normal spinel transition nor the transformation to h-Fe_3O_4 at pressures up to 21 GPa. On the other side Bengtson et al. (2013) predict in a theoretical ab-initio study a phase transition from inverse-spinel magnetite to h-Fe_3O_4 at 10 GPa. According to them there is no inverse- to normal-spinel transition in magnetite.

The symmetry of h-magnetite, initially interpreted as monoclinic (Pasternak et al., 1994) has also been subject of controversy. In a synchrotron X-ray diffraction study study Fei et al. (1999) found that h-Fe_3O_4, is not monoclinic but isotypic with $CaMn_2O_4$ (space group *Pbcm*), with all Fe^{3+} ions in octahedral sites and Fe^{2+} in eight fold-coordinated sites, which are described as bicapped trigonal prisms. Haavik et al. (2000) pointed out that their X-ray data were also consistent with the $CaTi_2O_4$ structure-type (space group *Bbmm*). Space group *Bbmm* for the h-Fe_3O_4 structure has been confirmed by Lazor et al. (2004), Dubrovinsky et al. (2003) and Bengtson et al. (2013). Dubrovinsky et al. (2003) suggest that Fe^{2+} occupies trigonal prism (Fe1) with an average Fe1-O distance of 2.058 Å and that Fe^{3+} occupies octahedra (Fe2) with average Fe2-O distance of 1.961 Å.

The high-pressure Fe-oxide, Fe_4O_5 is stable from 5 to at least 30 GPa, and is recoverable to ambient conditions (Lavina et al. (2011). They synthesized Fe_4O_5 in a pure Fe-O system, using mixtures of Fe and Fe_3O_4 as starting material, at $P = 10$ and 20 GPa, and T between 1227 and 1927 °C and refined the structure as isostructural with $CaFe_3O_5$ (space group *Cmcm*). In the proposed structure the atomic arrangement consists of two non-equivalent, edge-sharing FeO_6 octahedra (Fe1 and Fe2), which form layers perpendicular to the *c*-axis, alternating with layers of face-sharing trigonal prisms (Fe3). Thus, the structure is very

similar to h-Fe_3O_4. Lavina et al. (2011) speculate that synthetic Fe_4O_5 may show stacking disorder involving Fe_4O_5 and h-Fe_3O_4 octahedral layers may occur. In an in-situ high-pressure X-ray diffraction study, Woodland et al. (2012) observed that cubic magnetite breaks down to a mixture of hematite and Fe_4O_5 between 9.5 to 11 GPa and 700 to 1400 °C, in disagreement with Schollenbruch et al. (2011) who observe an isochemical transition to h-magnetitte in the same pressure and temperature regime. Woodland et al. (2012) suggested that the two coexisting phases, hematite and Fe_4O_5, recombine at higher pressures to form h-Fe_3O_4. Woodland at al. (2013) investigated the stability of Fe_4O_5 in several simple chemical systems and they found, e.g. that Fe in the Fe_4O_5 phase can be substituted by considerable amounts of other cations, e.g. Cr^{3+}.

Until now, h-Fe_3O_4 has been investigated only as a pure Fe-oxide and it has never been recovered at ambient conditions. There is no information about $Fe^{3+}/\Sigma Fe_{tot}$ ratio and possible incorporation of cations other than iron. Here we report crystal-chemical and structural data of this high-pressure Fe-oxide synthesized at 18 GPa and 1800 °C using (i) an oxide mixture with a SiO_2 concentration close to that of the bulk silicate Earth (O'Neill and Palme1998) and (ii) a Fe-dominated oxide mixture plus Cr-, Mg- and Si-oxides. Surprisingly the structure was quenchable in both types of experiments to ambient conditions, which allowed us to collect precise electron diffraction data by automated electron diffraction tomography (ADT). With this technique we were able to deliver crystallographic information for single nanocrystalline domains in a polyphasic mixture. We observe that h-magnetite coexisting with the silicates is strongly enriched in Cr, and we speculate on the effects that such partitioning might impose on the concentration of Cr in the coexisting silicates and in melts produced in the deep mantle.

Experimental methods

A. Synthesis

We performed three multi-anvil runs with a 10/5 assembly, rhenium heater, and type C thermocouples at P = 18 GPa and T = 1800 °C for 6 hours. Two experiments, MA-367 and MA-380, used a homogenous oxide mixture with 44.6 wt% SiO_2, 19.3 wt % MgO (annealed at 1200 °C), 15.7 wt % FeO, 17.1 wt % Al_2O_3 and 3.3 wt % Cr_2O_3 placed in Fe-doped Pt-capsules (about 3 wt% Fe) to reduce the potential loss of Fe (e.g. Grove 1981). In these two runs we produced assemblages with majorite as the major phase and three additional minor phases: stishovite, magnesite, and a Fe-oxide with the composition given in Table 1. We intentionally did not remove traces of adsorbed water or CO_2 in the starting materials as this may have served as a flux to enhance the growth of large crystals. The presence of water explains the formation of traces of magnesite in the run products and goethite as alteration product during quenching (see below). In order to achieve large crystals in the second run (MA-380), the temperature of 1800 °C was cycled by 20 °C for the first 30 min of the run duration. The starting material of the third run was a homogenous oxide mixture with 42 wt. % FeO, 34 wt. % Fe_2O_3, 13 wt. % Cr_2O_3, 6 wt. % Al_2O_3 and 5 wt. % SiO_2 also placed in Fe-doped Pt-capsules to reduce the potential loss of Fe. At the end of all runs temperature was quenched to ambient conditions within 2 minutes, and the decompression time was 43 hours to avoid breakage of the WC cubes. The 10/5 assembly was calibrated using the following phase transitions: coesite–stishovite (Akaogi et al. 1995), α–β Mg_2SiO_4 (Morishima et al. 1994), β–γ Mg_2SiO_4 (Inoue et al. 2006), enstatite–β Mg_2SiO_4–stishovite (Gasparik 1989). All the syntheses were performed at the high-pressure laboratory of the German Research Centre for Geosciences (GFZ) in Potsdam.

B. Electron microprobe analyses

Multi-phase aggregates of products from all three experiments were embedded in epoxy and polished for the electron microprobe (EMP) measurements. The chemical composition of the phases was determined by wavelength-dispersive X-ray analysis (WDS) techniques using a JEOL JXA-8500F (HYPERPROBE) electron microprobe at the GFZ in Potsdam. The

analytical conditions included an acceleration voltage of 15 kV, a beam current of 20 nA, and a beam diameter of 1 μm. The following natural and synthetic standards were used (with the respective element and peak counting time listed in parentheses): diopside (for Mg; 40 s, Si; 40 s, Ca; 40 s), hematite (for Fe; 40 s) and Cr_2O_3 (for Cr; 40 s). The background counting times were always set to half of the respective peak counting times. The CITZAF routine in the JEOL software was used for data processing. Element distribution maps were produced in WDS mode using an accelerating voltage of 15 kV and a beam current of 20 nA. We accumulated a 500 × 400 pixel frame with a step size of 0.5 μm and a dwell time of 200 ms per pixel in stage-scanning mode. We could not obtain satisfactory analyses of magnesite, which was instead identified by Raman spectroscopy (Fig S1), because it was not stable under the electron beam.

C. X-ray diffraction

X-ray diffraction patterns of compact multi-phase aggregates of the run products MA367 and MA376 about 100 μm in size were collected using a Rigaku R/AXIS200 SPIDER diffractometer operating at 40 kV and 30 mA at GFZ. The samples were mounted on CryoLoops (Hampton Research), and the loops were placed into a goniometer. During data acquisition the goniometer holding the sample was rotated continuously at a speed of 2 ° per second over 360°. A rotating Cu anode served as the X-ray photon source. The detection system consists of a cylindrically shaped image plate, which reads out the diffracted radiation in a 2θ range of – 60 to 144° in horizontal and +/- 45° in vertical direction. LeBail refinement was done using the GSAS software package (Larson & Van Dreele, 1998). Starting values for the refinements were the fractional atomic coordinates and lattice parameters for majorite, stishovite, and magnesite taken from the ICSD database (Belsky et al. 2002), the inorganic structure database. For h-Fe_3O_4 we used the results obtained from our automated electron diffraction tomography analyses (ADT). Powder XRD patterns for MA-376 were also recorded in transmission using a STOE STADI P diffractometer (Cu$K\alpha_1$ radiation), equipped with a primary monochromator and a 7°-wide

position sensitive detector at the GFZ Potsdam. A part of the run product was ground to a final grain size of about 5 μm, diluted with Elmer's white glue and spread on a circular amorphous foil. The foil was placed into a transmission sample holder and covered with a second foil. Intensities were recorded in the range of 2Θ from 9° to 125° with a detector step size of 0.1° and a resolution of 0.02°. A 1 mm thick Al-foil was placed in front of the detector in order to reduce fluorescence radiation in the Fe-rich sample. Counting time was selected to yield a maximum intensity of 5000 counts. Unit cell were refined using the GSAS software package for LeBail refinements (Larson & Von Dreele, 1987). Starting values for the refinements were the fractional atomic coordinates and lattice constants for h-Fe_3O_4 from our ADT analyses.

D. Transmission electron microscopy

Electron-transparent foils of sample MA-367 and MA-376 for transmission electron microscopy (TEM) were prepared at the TEM Laboratory of the GFZ by a focused ion beam (FIB) milling technique (Wirth 2009). Foils with the dimensions 15 × 10 × 0.150 μm were cut with a FEI FIB200TEM device using Ga-ions accelerated to 30 keV from the polished section of the sample on spots which were identified as Fe-oxide.

Automated electron diffraction tomography (ADT) was carried out with a FEI TECNAI F30 ST transmission electron microscope operating at 300 kV at the Johannes Gutenberg-Universität in Mainz. ADT has already been used for the structure characterization of high-pressure experimental products, like the hydrous Al-bearing pyroxene HAPY (Gemmi et al. 2011). We investigated both, FIB foils from MA367 and MA376 and micrometric grains (μ-crystals) selected with a micromanipulator. Samples were deposited on carbon-coated copper grids. In total nine ADT data sets were collected from MA-367 (four sets from μ-crystals and five sets from different areas of the FIB foil) and eight ADT data sets were collected from sample MA-376 (three sets from μ-crystals and five sets from different areas of the same FIB foil).

ADT was carried out using the automatic module described in Kolb et al. (2007). Each ADT data collection was performed in tilt steps of 1°, for total tilt ranges of 90-120°. Electron diffraction patterns were acquired in nano-beam electron diffraction (NED) mode, with a quasi-parallel illumination obtained using a condenser aperture (C2) of 10 µm. The beam on the sample had a diameter of 70 nm. Crystal position was tracked after each tilt step in µ-probe scanning transmission electron microscopy (µ-STEM) mode. Data sets were collected both with and without precession of the beam (precession electron diffraction – PED for details see Vincent and Midgley, 1994; Mugnaioli et al. 2009). Data sets without precession were used for accurate cell parameter determination, while data sets with precession were used for reflection intensity extraction.

ADT data were analyzed using the ADT3D software (Kolb et al. 2008; Mugnaioli et al. 2009; Kolb et al. 2011; Schlitt et al. 2012), including three-dimensional diffraction reconstruction and visualization, cell determination and reflection intensity integration. Ab-initio structure solution was performed by direct methods using SIR2011 (Burla et al. 2012).

Conventional in-zone electron diffraction patterns were recorded on the FIB-foils in a Tecnai F20-X-Twin microscope with a field emission gun as the electron source at the TEM Laboratory of the GFZ in Potsdam. The TEM is equipped with a Gatan imaging filter (GIF Tridiem), a Fishione high-angle annular dark field detector (HAADF), and an EDAX X-Ray analyzer. Energy-dispersive spectra were collected for 30 s on different spots of the sample to identify the phase of interest and to ensure that the additional elements are intrinsic to the Fe-oxide. Electron diffraction patterns were recorded from these sites with image plates. Fe^{3+} concentration was determined with electron energy-loss spectroscopy (EELS), applying the technique described by van Aken and Liebscher (2002). Spectra were acquired in the diffraction mode with a camera length of 700 mm. Convergence angle was 2 mrad, and the collection angle at the camera length used was 10 mrad with a GIF entrance aperture of 2 mm.

Dispersion was 0.1 eV/ channel. The energy resolution of the filter was 0.9 eV at full-width at half maximum of the zero loss peak.

FTIR spectroscopy

To check for the presence of intrinsic OH, IR spectra were taken at the FTIR Laboratory to the GFZ on single crystals of majorite and multiphase aggregates containing the Fe-oxide from run MA-380. Spectra were recorded on a Bruker Vertex 80v FTIR spectrometer, equipped with a Globar light source, a KBr beam-splitter and a Hyperion microscope using Cassegrainian objective and an InSb detector. Spectra were taken with aperture sizes depending on the crystal and aggregate size from 50 × 50 to 50 × 100 μm and a resolution of 2 cm^{-1}. Spectra were averaged over 256 scans.

Results

Optical analyses of the products of MA-367 in transmitted light revealed that the major phase is a yellowish, isometric phase up to 30 μm in diameter, identified later as majorite, accompanied by an opaque phase, often appearing as elongated aggregates with 10 to 30 μm long and later identified as h-Fe_3O_4. In addition, we identified two additional colorless phases, stishovite and magnesite, of the same small size. The same phases were also identified in the second run MA-380. In the latter, the majorite crystals were on average much larger than in sample MA-367, (up to 100 μm). Obviously, *T*-cycling of the run produced larger single crystals of the garnet phase. Optical examination of the products of MA-376 in transmitted light revealed that it is completely opaque powder.

Electron microprobe analyses

Electron microprobe analyses confirmed that the product of run MA-367 consist of four phases: majorite ($Mg_{1.98}Fe_{1.05}(Al_{1.61}Cr_{0.11}Si_{0.11}Mg_{0.16})Si_3O_{12}$), nearly pure stishovite ($Si_{0.98}Al_{0.02})O_2$, a carbonate with composition of ($Mg_{0.8}Fe_{0.2})CO_3$, and a Cr-, Mg-, Al- and Si-containing Fe-oxide (Fig. 1 a, c; Tab. 1). According to the results of the TEM analysis the normalization procedure for the Fe-oxide was performed on the base of four oxygens and to

account for the presence of Fe^{3+}, we assumed the stoichiometry ΣM/O = 0.75. The calculated formula for the Fe-oxide is $(Fe^{3+}_{1.39}Fe^{2+}_{0.75}Cr_{0.29}Mg_{0.26}Al_{0.21}Si_{0.08})_{\Sigma=3}O_4$. The microprobe analyses of magnesite showed a relatively constant composition of about $Mg_{0.8}Fe_{0.2}CO_3$ (based on six analyses). The presence of ferroan magnesite as an impurity has been confirmed by Raman spectroscopy (the Raman peaks are shifted to lower wavenumbers compared to the pure magnesite end-member, thus confirming Fe-Mg substitution; Fig. S1 deposited item). Electron microprobe analyses further revealed that the run products of MA-380 consist of Mg-rich majorite, nearly pure stishovite $(Si_{0.98}Al_{0.02})O_2$, and a Cr-, Mg-, Al- and Si-containing Fe-oxide (Fig. 1 b). The crystal size of the Fe-oxide phase in the polished section of run MA-380 was too small to obtain sufficiently good chemical analyses, and the oxide sums are always approximately around 90%.

Electron microprobe analyses revealed that the product of run MA-376 consist of three phases: the major phase is a Cr-, Al-, Si-, and Mg-containing Fe-oxide and in addition traces of stishovite and nearly pure Mg-end-member wadsleyite (Fig. 1d). The compositionof the Fe-oxide phase present in MA-376 is slightly different with respect to that in MA-367 as it does not incorporated magnesium and is thus more Fe-rich. The calculated formula for the Fe-oxide normalized to four oxygen is $(Fe^{3+}_{1.30}Fe^{2+}_{1.02}Cr_{0.37}Al_{0.25}Si_{0.05})_{\Sigma=3}O_4$.

X-ray diffraction and Transmission electron microscopy analyses

MA-367

We collected X-ray diffraction pattern on several aggregates of MA-367 using the Rigaku diffractometer and could identify majorite as the major phase plus stishovite plus magnesite. Some pattern showed weak reflections at about $2\Theta_{Cu}$ 33.2°, 33.8° and 37.5 -37.6° (listed by decreasing intensity), which could not be explained either with the phases mentioned above or with other known oxide phases. Therefore the Fe-oxide phase of the sample was further investigated using automated electron diffraction tomography. ADT data revealed that the sample MA-367 contains two different Fe-oxide phases, which we call α-phase and β-phase

for simplicity. The α-phase is always predominant compared to the β-phase. Data acquired from μ-crystals show that the two phases usually appear together and that the diffraction images contain strong signals of the α-phase in addition to weaker signals from the β-phase. However, in the FIB foils it was possible to recognize areas where the two phases are clearly separated and in these areas it was possible to acquire ADT data from each of them. Fig. 2 shows a high-angle annular dark-field image (HAAD) image (camera length 330 mm) of a FIB foil cut from a Fe-oxide grain of this sample. Fe-oxide grains consist of coherent areas of α-phase, separated by planar deformation features filled with the β-phase.

ADT structure analysis of the α-phase: Detailed analyses of the ADT data sets of sample MA-367 revealed that the α-phase crystallizes in the h-magnetite structure (Haavick et al. 2000 in-situ X-ray powder diffraction (XRPD) at P > 22 GPa). This was a surprise because h-magnetite is known to be unquenchable to ambient condition. All ADT data sets taken on the α-phase were consistent with an orthorhombic cell with parameters a = 9.8(2) Å, b = 9.6(2) Å, c = 2.87(6) Å (Fig. 3 a and b). These values are close to the cell parameters determined for *h*-Fe_3O_4 by Haavick et al. (2000) on the basis of XRPD. The analysis of the three dimensional reconstructed diffraction volumes revealed always the presence of two main extinction rules: $hkl : k + l = 2n$ and $h0l : h = 2n$, consistent with space groups *Amam*, *Ama*2 and $A2_1am$ (Tab. 2). These extinction rules are not consistent with Haavick's space group *Bbmm*. *Amam* and *Bbmm* are both not conventional settings of space group *Cmcm* (63), but represent physically different objects when the cell parameter setting is fixed (in our case a='long', b='medium', c='short'). The difference between our ADT and Haavick's findings can be reconciled exchanging the a and b parameter. There are two possible explanation for this difference: i) there is a real structural modification related with the introduction of Mg and Cr and/or the quenching of the material; ii) there is an error in the determination of cell parameters or extinctions either by ADT or XRPD data. We point out that, despite the high error (2%) related with a single ADT cell determination (Kolb et al. 2011), the evidence that a is always

longer than *b* and that the presence of extinctions consistent with space group *Amam* were always confirmed by all the independent ADT acquisitions. On the other hand, in presence of close *a* and *b* cell parameters and low quality XRPD data (as the ones available by Haavick et al. 2000), it is not trivial to discriminate between space groups *Amam* and *Bbmm*. For a matter of clarity, we report in Tab. 2 the extinction rules associated with these two space groups. Swapping *a* and *b* axes, the two space groups can be exchanged. According with the orthorhombic setting, reflection intensities were integrated for the two best ADT acquisition series, both performed with beam precession (Mugnaioli et al. 2009). Experimental details are given in Tab. 3. Ab-initio structure solution was performed independently for the two data sets by direct methods implemented in SIR2011 (Burla et al. 2012), using scattering factors for electrons (Doyle and Turner 1968) and kinematic approximation (I_{hkl} proportional to F_{hkl}^2). Structure solution converged in space group *Amam*. Only the solution automatically picked by the SIR2011, i.e. the one with the lowest residual, was considered. The resulting potential maps (Tab. 4) show two strong maxima followed by three weaker maxima. The first two positions were interpreted as iron and the following three as oxygen atoms. In spite of the different space group, the structure achieved by ADT is in fact very close to the one refined by XRPD (Haavick et al. 2000). The structure was subsequently refined by least-squares using SHELX97 (Sheldrick 2008) including partial occupancy of iron/magnesium and iron/chromium in the octahedral sites (cif file in deposit item). Only soft "SADI" restraints (σ = 0.05 Å) were applied to Fe-O distances, independently for each Fe atom. The model obtained ab-initio remains stable upon refinement with SHELXL but the refinement does not converge better than to $R1_{all}$ = 33.83% (Tab. 3). Structure residuals and GooF are rather high when compared with X-ray diffraction, but typical for electron diffraction data (Kolb et al. 2011). In the present case dynamical effects and structure residuals are emphasized by the high density of the material and the thickness of the samples -estimated about 200-400 nm for μ-crystals and 150 nm for the FIB cuts- (Kolb et al. 2011; Jacob et al. 2013). Fe^{3+} occupies a

337 nicely symmetrical octahedron, while Fe^{2+} is hosted inside a trigonal prismatic coordination
338 as suggested by Dubrovinsky et al. (2003). Results and reliability of structure refinement by
339 (ADT) electron diffraction data for an accurate determination of interatomic distances and
340 partial occupancies have been recently reported and discussed by Birkel et al. (2010),
341 Pignatelli et al. (2014) and Jacob et al. (2013), using either kinematical and dynamical
342 approaches. Here, we stress that in agreement with crystallochemical expectations and with
343 the results of Dubrovinsky et al. (2003) Fe-O distances related to Fe^{3+} are significantly shorter
344 compared with the ones related to Fe^{2+} (<2.04> Å vs. <2.14> Å). This is not the case for the
345 structure refined by Haavick et al. (2000), where interatomic Fe^{2+}-O distances in the trigonal
346 prismatic coordination vary significantly. Partial occupancies Fe/Cr and Fe/Mg of the Fe sites
347 were refined up to values close to the ones estimated by WDS. While the former converged to
348 similar values for both the refinements, the latter showed a large deviation.
349 Identification of the β-phase: Detailed analyses of the ADT data sets of MA-367 revealed that
350 the β-phase is most likely isostructural with goethite FeOOH (Yang et al. 2006), which is also
351 confirmed by a preliminary structure solution based on the ADT data. It has a primitive
352 orthorhombic cell with parameters a = 4.6(1) Å, b = 9.5(2) Å, c = 3.00(6) Å. Extinctions are
353 consistent with space group *Pbnm*. When α-phase and β-phase are present together they
354 always have orientation relations with $a(\alpha) // b(\beta)$, $b(\alpha) // a(\beta)$ and $c(\alpha) // c(\beta)$ (Fig. 3 c and
355 d). The main feature for distinguishing the two phases is the different length of the cell
356 parameter c.
357 The unknown reflections observed in the X-ray diffraction pattern of MA-367 can be
358 explained as reflections of h-magnetite with the cell parameters determined based on our
359 ADT analysis.
360 High resolution TEM confirmed that the Fe-oxide phase produced in run MA-367 is h-
361 magnetite quenched to ambient conditions. It also confirmed the presence of a second phase,
362 which we did not further investigated with high resolution TEM. We measured the reciprocal

lattice vectors in the TEM diffraction pattern and calculated the respective *d*-spacings and angles between adjacent vectors or lattice plane. The analyses were performed with selected area electron diffraction (SAED) patterns in different orientations (zone axes). The diffraction images are shown in Figure 4a and can be indexed as h-Fe_3O_4 along the [-21-1] zone axis. The basis for the indexing was the set of lattice parameters and structure obtained from the ADT analyses for h-magnetite. With the high resolution TEM we only confirm the presence of h-magetite we cannot prove the space group. Table 5 shows the observed *d*-spacings and corresponding angles between vectors for both samples. In our TEM analyses both in Mainz and at the GFZ we systematically supplemented electron diffraction with energy-dispersive X-ray spectroscopy (EDX) performed in the same locations of the foils. All the EDX measurements always yielded the same proportions of Cr, Mg, Al, and Si and there was no clear difference between the composition of the α-phase and β-phase.

In addition, we measured EEL spectra of the Fe $L_{2,3}$-edges of h-magnetite of run MA-367 and compare them to the spectrum of a synthetic majorite by Lenz et al. (2012) (Fig. 6). The spectrum of the iron oxide does not show the characteristic L_3 splitting that is present for majoritic garnet (Fig. 6). In addition the maxima of the L_3 and L_2 egdes are shifted to lower energy compared to cubic magnetite, e.g. the maximum of the L_3 of magnetite lies at 709 eV (van Aken and Liebscher 2002). Applying the calibration by van Aken and Liebscher (2002) the averaged Fe^{3+}/Fe_{total} ratio for both phases was approximately 25% (eight analyses), which is, in the case of majorite, in the range expected from other experiments (Stagno et al. 2013), but much too low for h-magnetite (Tab. 1). Crocombette et al. (1995), Van Aken and Liebscher (2002) and Gloter et al. (2003) observed for magnetite an unsplitted broad but asymmetric L_3 peak at about 709 eV. They attribute this feature to strong charge-transfer interactions between ferrous and ferric iron (electron hopping). Thus, the calibration of van Aken and Liebscher (2002) cannot be used to quantify the Fe^{3+} content in the oxides of our run products.

MA-376

Sample MA-376 consists of about 95% Fe-oxide phase. In this sample the Fe-oxide phase presents defect density, deformation features, and region characterized by poor crystallinity. In addition, in spite of our efforts to isolate it from atmospheric moisture, the oxide phase appears to suffer progressive weathering. We collected X-ray diffraction pattern on several opaque aggregates of MA-376 with the Rigaku diffractometer at the GFZ. The diffraction patterns (from integration of the single images) were dominated by two peaks at $2\Theta_{Cu}$ 32.7 ° and 34.3 °. However, the intensity ratios of the two peaks vary very strongly from image to image, which may indicate a strong texture effect. To get information on the whole sample we ground several aggregates and prepared them properly for the STOE transmission diffractometer. The X-ray diffractogram and the results of a LeBail refinement are shown in Fig. 5. The X-ray pattern of the Fe-oxide phase in MA-376 can be explained with h-magnetite with slightly different lattice constant of a = 9.99 b = 9.58 and c = 2.83 Å. We did not observe reflections of goethite. This is likely due to the relative small volumetric amount of β-phase. Additionally, β-phase crystallizes in tiny nanocrystals and its cell parameters are related with cell parameters of h-magnetite. The resultant peak enlargement and overlap make β-phase signal almost completely hidden by the stronger h-magnetite signal. The final R_{Bragg} value was 1.7 %. A list of the intensity extraction (hkl) is shown in Tab S1 (deposit item). Finally we investigated the sample with ADT and HR-TEM. Both methods confirm the presence of h-magnetite but also indicate that the sample has a high defect density and cannot be used for structure determination. The diffraction image of the Fe-oxide from the foil of run MA-376 measured with HR-TEM is shown in Figure 4b and can be indexed as h-Fe_3O_4 viewed along the [001] zone axis. The ADT data sets revealed again the presence of goethite in larger amounts than in MA-367 and the same oriented intergrowth with h-magnetite.

FTIR-Spectroscopy

The total amount of hydrogen incorporated in majorite of run MA-380 has been quantified as 1000 ppm H_2O by weight by comparing the IR spectra with spectra of a synthetic majorite (Lenz et al. 2012) containing 2200 ppm H_2O by weight (Fig. 6,).

Discussion

TEM analyses show that the Fe-oxide in our high-pressure run products crystallized in the structure of h-Fe_3O_4 and are quenchable to ambient conditions and stable under the experimental condition of most of the measurements (X-ray, electron beam). Microprobe analyses are consistent with about 62% of the Fe_{total} incorporated as Fe^{3+}. Electron microprobe (WDS) along with analytical TEM analyses reveal that the Fe-oxide incorporated significant amounts of Cr, Mg, Al and Si. We assigned the divalent cations to the larger Fe1site and the three and four-valent cations to the smaller octahedral site Fe2 (Dubrovinsky et al. 2003). This is also supported by ADT analyses. Hence we propose the following structural formula for the high-pressure Fe-oxide synthesized here: $^{Fe1}(Fe^{2+}_{0.75}\ Mg_{0.26})\ ^{Fe2}(Fe^{3+}_{0.70}\ Cr_{0.15}Al_{0.11}\ Si_{0.04})_2O_4$ for MA-367 and $^{Fe1}(Fe^{2+}_{1.02})\ ^{Fe2}(Fe^{3+}_{0.65}\ Cr_{0.19}Al_{0.13}\ Si_{0.03})_2O_4$ for MA-376.

In MA-367 the Fe-oxide forms hypidiomorphic elongated aggregates10 – 30 μm long, mutually intergrown with majorite, the major phase of the run products. The texture of our "synthetic rock" composed of majorite, stishovite, h-Fe3O_4 and magnesite (Fig. 1) and the rather uniform chemical compositions of the phases suggests that they have attained equilibrium. It is difficult to estimate the redox conditions in terms of f_{O2} during the experiment. But at least the presence of magnesite gives us a minimum value: according to Stagno et al. (2011) at 18 GPa and *T* between 1500 and 1700 °C an f_{O2} of at least 3 log units above IW is required to prevent the reduction of magnesite to diamond and MgO. Thus, we estimate that the f_{O2} in the experimental charge was near the magnetite-wüstite buffer (that is 3-4 log units above IW). It is clear that the coexisting majorite must also incorporate Fe^{3+} to some extent; however, for simplicity, the Fe pfu for the majorite phases of this study were calculated assuming ferrous iron only. As shown in Fig. 6 for a majorite of similar

composition and synthesized in the experiment MA-337 under similar conditions (Lenz et al. 2012), 25% of the total Fe can be assumed to be Fe^{3+}.

The same holds true for MA-380, in which we succeeded in crystallizing large crystals by T-cycling in the first heating phases.

In MA-376 the h-magnetite is more Fe-rich than in MA367. It has no magnesium incorporated in the Fe1site. The oxide phase tends to decompose with time, maybe due to its Fe-richer composition. However, the transformation is not abrupt as known for the pure Fe-end-member. One and a half year after the synthesis we could still prove its presence. Compared to MA367, the products of run MA-376 include the end-member wadsleyite, which stores all the Mg present in the starting material. As h-magnetite in run MA-367 did incorporate Mg and did coexist with Fe, Mg – silicates we tend to interpret this observation as non-equilibrium.

The presence of small amounts of goethite was only observed in the ADT data sets neither in our X-ray diffraction data nor EMP analyses. From the oriented intergrowth with h-magnetite it is clear that theis a secondary phase, which was formed most likely during quenching. Although we did not add pure water to the sample the powder contained adsorbed water as proven by the OH incorporation in the majorite crystals.

Implications

We report the synthesis of h-magnetite, ideally h-Fe_3O_4 with considerable amounts of substitutional cations (Cr, Mg, Al, Si) and quenchable to ambient conditions. The substitution of Fe by smaller cations may stabilize the high-pressure form during quenching. If this is true similar substitution mechanisms can be applied to other non-quenchable high-pressure phases to recover them for better crystal chemical and structural characterization.

Our experiments suggest that h-magnetite is a potential constituent of the Earth's mantle. It can incorporate large amounts of Cr, Mg, Al and Si and the most of its iron is Fe^{3+}. The preservation of mantle heterogeneity as relicts of materials (most likely related to ancient

466 subduction) that are not thermally and/or chemically equilibrated with the ambient mantle is
467 suggested by seismic observations, and is consistent with mineral physics results, even in the
468 deep mantle (Mosenfelder et al., 2001; Kaneshima et al., 2007; Bina, 2010; Vinnik et al.,
469 2010). Heterogeneities and anomalies observed at the transition zone level can be connected
470 to fragments of ancient subducted lithosphere not yet thermally equilibrated where Fe-
471 enriched, oxidized lithospheric material could be intermixed with remnants of carbonatic
472 sediments (Nolet and Zielhuis, 1994; Courtier and Revenaugh, 2007). In such environments,
473 before complete equilibration, local redox conditions may be more oxidized than that of the
474 ambient mantle. Our syntheses performed at transition-zone pressures show that h-magnetite-
475 is stabilized in equilibrium with Fe-rich majoritic garnet at f_{O_2} close to the magnetite-wüstite
476 buffer (i.e. 3-4 log units above IW) in a simplified system comparable to a Fe-enriched
477 subducted lithospheric material. We observe that Cr is strongly enriched in the oxide phase
478 with respect to the coexisting majoritic garnet with a partitioning coefficient $D_{Cr}^{Oxide/Majorite}$ of
479 about 2.6. Our experimental results suggest that h-Fe_3O_4 can be considered as deep mantle
480 mineral (at least in special environments). Its formation may have consequences on the
481 chemical signature of coexisting silicates. Where h-Fe_3O_4 forms in the presence of residual
482 carbonates, such strong fractionation could be recorded in terms of the chemical signature of
483 silicate inclusions in deep diamonds associated with deep mantle carbonatitic melt production
484 (Rohrbach and Schmidt 2011; Stagno et al. 2013).
485 This work demonstrates the advantage of electron diffraction, and particularly of the ADT
486 method, for the structural analysis of phases that occur only as nano-sized crystals in
487 polyphasic assemblages, even when a limited amount of material is available. ADT method
488 also allows to recover geometrical information at the nano scale, like the reciprocal
489 orientation of goethite and h-Fe_3O_4 intergrowth in the Fe-oxide grains.
490
491

Acknowledgments

We thank A. Schreiber, U. Dittmann, A. Ebert, R. Schulz and H.-P. Nabein for technical support and Wilhelm Heinrich for discussion. We also thank Barbara Lavina, Ian Swainson, Oliver Tschauner and an anonymous reviewer for their comments.

References

Akaogi, M., Yusa, H., Shiraishi, K., and Suzuki, T. (1995) Thermodynamic properties of alpha-quartz, coesite and stishovie and equilibrium phase relations at high pressures and high temperatures. Journal of Geophysical Research, 100, 337 – 347.

Belsky, A., M. Hellenbrandt, V.L. Karen, and P. Luksch (2002) New developments in the Inorganic Crystal Structure Database (ICSD): accessibility in support of materials research and design. Acta Cryst., B58, 364-369.

Bengtson, A., Morgan, D., and Becker, U. (2013) Spin state of iron in Fe_3O_4 magnetite and h-Fe_3O_4. Physical Review B87, 155141-1 – 155141-13.

Bina, C.R. (2010) Scale limits of free-silica seismic scatterers in the lower mantle. Physics of the Earth and Planetary Interiors, 183, 110-114.

Birkel, C. S., Mugnaioli, E., Gorelik, T., Kolb, U., Panthöfer, M., and Tremel, W. (2010) Solution Synthesis of a New Thermoelectric $Zn_{1+x}Sb$ Nanophase and Its Structure Determination Using Automated Electron Diffraction Tomography. Journal of the American Chemical Society, 132, 9881-9889.

Bowles, J.F.W., Howie, R.A., Vaughan, D.J., and Zussman, J. (2011) Deer, Howie, and Zussman Rockforming Minerals Non Silicates 5A, Second edition, published by the Geological Society of London, ISDN 978-1-86239-315-8, ISSN 2041-6296, 927 pages.

Burla, M.C., Caliandro, R., Camalli, M., Carrozzini, B., Cascarano, G.L., Giacovazzo, C., Mallamo, M., Mazzone, A., Polidori, G., and Spagna, R. (2012) *SIR2011*: a new package for

517 crystal structure determination and refinement. Journal of Applied Crystallography, 45, 357-
518 361.
519 Courtier, A.M. and Revenaugh, J. (2007) Deep upper-mantle melting beneath the Tasman and
520 Coral Seas detected with multiple ScS reverberations. Earth and Planetary Science Letters,
521 259, 66-76.
522 Crocombette, J.P., Pollak, M., Jollet, F., Thromat, N., and Gautier-Soyer, M. (1995) X-ray-
523 absorption spectroscopy at the Fe $L_{2,3}$ threshold in iron oxides. Physical Review B, 52, 3143 –
524 3150.
525 Doyle, P. A., and Turner, P. S. (1968) Relativistic Hartree-Foek X-ray and Electron Scattering
526 Factors. Acta Crystallographyca A, 24, 390-397.
527 Dubrovinsky, L. S., Dubrovinskaia, N. A., McCammon, C., Rozenberg, G. K., Ahuja, R.,
528 Osorio-Guillen, J. M., Dmitriev, V., Weber, H. P., Le Bihan, T., and Johansson, B. (2003)
529 The structure of the metallic high-pressure Fe_3O_4 polymorph: experimental and theoretical
530 study. Journal of Physics-Condensed Matter, 15, 7697-7706
531 Fei Y., Crystal chemistry of FeO at high pressure and temperature (1996) in Mineral
532 Spectroscopy: A Tribute to Roger G. Burns. Edited by M.D. Dyar, C. McCammon, and M.W.
533 Schaefer, 243-254.
534 Fei, Y., Frost, D.J., Mao, H.-K., Prewitt, C., and Häusermann, D. (1999) In situ structure
535 determination of the high-pressure phase of Fe_3O_4. American Mineralogist, 84, 203 – 206.
536 Fei, Y., and H.K. Mao (1994) In-situ determination of the NiAs phase of FeO at high-pressure
537 and temperature. Science, 266, 1678-1680.
538 Fisher, R.A., Campbell, A.J., Shofner, G.A., Lord, O.T., Dera, P., and Prakapenka, V.B.
539 (2011) Equation of state and phase diagram of FeO. Earth and Planetary Science Letters, 304,
540 496-502.
541 Gasparik, T. (1989) Transformation of enstatite – diopside – jadeite pyroxenes to garnet.
542 Contribution to Mineralogy and Petrology, 102, 389 – 405.

Gemmi, M., Fischer, J., Merlini, M., Poli, S., Fumagalli, P., Mugnaioli, E. and Kolb, U. (2011) A new hydrous Al-bearing pyroxene as a water carrier in subduction zones. Earth and Planetary Science Letters, 310, 422–428.

Gloter, A., Douiri, A., Tencé M., and Colliex, C. (2003) Improving energy resolution of EELS spectra: an alternative to the monochromator solution. Ultramicroscopy, 96, 385 – 400.

Glazyrin, K., McCammon, C., Dubrovinsky, V., Merlini, M., Schollenbruch, K., Woodland, A., and Hanfland, M. (2012) Effect of high pressure on the crystal structure and electronic properties of magnetite below 25 GPA

Grove, T.L. (1981) Use of FePt alloys to eliminate the iron loss problem in 1 atompshere gas mixing experiments: theoretical and practical considerations. Contributions to Mineralogy and Petrology, 78, 298 – 304.

Haavik, C., Stølen, S., Fjellvåg, H., Hanfland, M., and Häusermann, D. (2000) Equation of state of magnetite and its high-pressure modification: thermodynamics of the Fe-O system at high pressure. American Mineralogist, 85, 514 – 523.

Hazen, R.M., and R. Jeanloz (1984) Wüstite (Fe1-xO): A review of its defect structure and physical properties. Reviews of Geophys. Space Phys., 22, 37-46.

Huberty, J.M., Konishi, H., Heck, P.R., Fournelle J.H., Valley, J.W., and Xu, H. (2012) Silician magnetite from the Dales Gorge Member of the Brockman Iron Formation, Hamersley Group, Western Australia. American Mineralogist, 97, 26–37.

Inoue, T., Irifune, T., Higo, Y., Sanehira, T., Sueda, Y., Yamada, A., Shinmei, T., Yamazaki, D., Ando, J., Funakoshi, K., and Utsumi, W. (2006) The phase boundary between wadsleyite and ringwoodite in Mg_2SiO_4 determined by in situ X-ray diffraction. Physics and Chemistry of Minerals, 33, 106 – 114.

Jacob, D., Palatinus, L., Cuvillier, P., Leroux, H., Domeneghetti, C., and Cámara, F. (2013) Ordering state in orthopyroxene as determined by precession electron diffraction. American Mineralogist, 98, 1526-1534.

569 Kaneshima, S., Okamoto, T., and Takenaka, H. (2007) Evidence of a metastable olivine
570 wedge inside the subducted Mariana slab. Earth and Planetary Science Letters, 258, 291-227.
571 Kantor, Y., A. Kurnusov, C. McCammon, and L. Dubrovinsky (2008) Monoclinic FeO at
572 high pressures. Z. Krist., 223, 461-464.
573 Kolb, U., Gorelik, T., Kübel, C., Otten, M.T., and Hubert, D. (2007) Towards automated
574 diffraction tomography: Part I—Data acquisition. Ultramicroscopy, 107, 507-513.
575 Kolb, U., Gorelik, T., and Otten, M.T. (2008) Towards automated diffraction tomography.
576 Part I— Cell parameter determination. Ultramicroscopy, 108, 763-772.
577 Kolb, U., Mugnaioli, E., and Gorelik, T.E. (2011) Automated electron diffraction tomography
578 – a new tool for nano crystal structure analysis. Crystal Research and Technology, 46, 542-
579 554.
580 Kondo, T., E. Ohtani, N. Hirao, T. Yagi, and T. Kikegawa (2004) Phase transitions of
581 (Mg,Fe)Oat megabar pressures. Phys. Earth Planet. Inter., 143-144, 201-213.
582 Larson, A.C. and Von Dreele, R.B. (1998) GSAS. General Structure Analysis System. Los
583 Alamos National Laboratory. Los Alamos, NM 87545. Copyright: The Regents of the
584 University of California.
585 Lavina, B., Dera, P., Kim, E., Meng, Y., Downs, R.T., Weck, P.F., Sutton, S.R., and Zhao, Y.
586 (2011) Discovery of the recoverable high-pressure iron oxide Fe_4O_5. Proceedings of the
587 National Academy of Sciences, 108, 17281 – 17285.
588 Lazor, P., Shebanova, O.N., and Annersten, H. (2004) High-pressure study of stability of
589 magnetite by thermodynamic analysis and synchrotron X-ray diffraction. Journal of
590 Geophysical Research, 109, B05201.
591 Lenz, S., Koch-Müller, M., Mrosko, M., Rhede, D., and Wirth, R. (2012): Crystal chemistry
592 of synthetic majoritic garnet. Conference Abstracts, 14th International Conference
593 Experimental Mineralogy Petrology Geochemistry - EMPG (Kiel, Germany 2012), 94.

Morishima, H., Kato, T., Suto, M., Ohtani, E., Urakawa, S., Utsumi, W., Shimomura, O., and Kikegawa, T. (1994) The phase boundary between α- and β-Mg_2SiO_4 determined by in situ X-ray observation, Science, 26, 1202 – 1203.

Mosenfelder, J.L., Marton, F.C., Ross II, C.R., Kerschhofer, L., and Rubie, D.C. (2001) Experimental constraints on the depth of olivine metastability in subducting lithosphere. Physics of the Earth and Planetary Interiors, 127, 165-180.

Mugnaioli, E., Gorelik, T., and Kolb, U. (2009) "Ab initio" structure solution from electron diffraction data obtained by a combination of Automated Diffraction Tomography and Precession Technique. Ultramicroscopy, 109, 758-765.

Nolet, G. and Zielhuis, A. (1994) Low S velocities under the Tornquist-Teisserye zone: evidence for water injection into the transition zone by subduction. Geophysical Research Letters, 99, 15813-15820.

O'Neill, H.St.C. and Palme, H. (1998) Composition of the Silicate Earth: Implications for Accretion and Core Formation. In: The Earth's Mantle, ed. I. Jackson, pp. 3-127. Cambridge University Press.

Ono, S., Kikegawa, T. and Ohishi, Y. (2004) High-pressure phase transition of hematite, Fe_2O_3. Journal of Physics and Chemistry of Solids, 65, 1527 – 1530.

Pasternak, M. P., Nasu, S., Wada, K., and Endo, S. (1994) High-pressure phase of magnetite. Physical Review B, 50, 6446 – 6449.

Pignatelli, I., Mugnaioli, E., Hybler, J., Mosser-Ruck, R., Barres, O., Kolb, U., and Michau, N. (2014) A multi-technique, micrometer- to atomic-scale description of a synthetic analogue of chukanovite, $Fe_2(CO_3)(OH)_2$. European Journal of Mineralogy, 26, 221-229.

Rohrbach, A., and Schmidt, M. (2011) Redox freezing and melting in the Earth's deep mantle resulting from carbon-iron redox coupling. Nature, 472, 209-212.

Schlitt, S., Gorelik, T.E., Stewart, A.A., Schömer, E., Raasch, T., and Kolb, U. (2012) Application of clustering techniques to electron diffraction data: determination of unit-cell parameters. Acta Crystallographica A, 68, 536–546.

Schmidt, E.R. and Vermaas, F.H.S. (1955) Differential thermal analysis and cell dimensions of some natural magnetites. American Mineralogist, 40, 422 – 431.

Schollenbruch, K., Woodland, A.B., Frost, D.J., Wang, Y., Sanehira, T., and Langenhorst, F. (2011) In situ determination of the spinel post-spinel transition in Fe_3O_4 at high pressure and temperature by synchrotron X-ray diffraction. American Mineralogist, 96, 820 – 827.

Shu, J., Mao, H.K., Hu, J., Fei, Y., and Hemley, R.J. (1998) Single-crystal X-ray diffraction of wüstite to 30 GPa hydrostatic pressure. Neues Jahrbuch für Mineralogie–Abhandlung, 172, 309-323.

Sheldrick, G. M. (2008) A short history of *SHELX*. Acta Crystallographyca A, 64, 112-122.

Stagno, V., Tange, Y., Miyajima, N., McCammon, C.A., Irifune, T. and Frost, D.J. (2011) The stability of magnesite in the transition zone and the lower mantle as function of oxygen fugacity. Geophysical Research Letters, 38, L19309.

Stagno, V., Ojwang, D.O., McCammon, C.A., and Frost, D.J. (2013) The oxidation state of the mantle and the extraction of carbon from Earth's interior. Nature, 493, 84-90.

Trots, D.M., Kurnosov, A., Woodland, A.B., and Frost, D.J. (2012) The thermal breakdown of Fe_4O_5 at ambient pressure. European Mineralogical Conference, 1, EMC2012-556-1, 2012.

Van Aken, P.A. and Liebscher, B. (2002) Quantification of ferrous/ferric ratios in minerals: new evaluation schemes of Fe L23 electron energy-loss near-edge spectra. Physics and Chemistry of Minerals, 29, 188 – 200.

Vinnik, L.P., Oreshin, S.I., Speziale, S., and Weber, M. (2010) Mid-mantle layering from SKS receiver functions. Geophysical Research Letters, 37, L24302.

642 Wirth, R. (2009) Focused Ion Beam (FIB) combined with SEM and TEM: Advanced
643 analytical tools for studies of chemical composition, microstructure and crystal structure in
644 geomaterials on a nanometre scale. Chemical Geology, 261, 3-4, 217-229.
645 Woodland, A.B., Frost, D.J., Trots, D.M., Klimm, K., and Mezouar, M. (2012) In situ
646 observation of the breakdown of magnetite (Fe_3O_4) to Fe_4O_5 and hematite at high pressures
647 and temperatures. American Mineralogist, 97, 1808 – 1811.
648 Woodland, A.B., Schollenbruch, K., Koch, M., Boffa Ballaran, T., Angel, R. J.,and Frost, D.
649 J. (2013) Fe4O5 and its solid solutions in several simple systems. Contrib. Mineral. Petrol,
650 166, 1677 – 1686.
651 Yang, H. X., Ren, L., Downs, R. T., Costin, G. (2012) Goethite, alpha FeO(OH), from single-
652 crystal data. Acta Crystallographica, section E. Structure reports online (2006) 62, pi250-
653 pi252.
654 Zou, G., Mao, H.K., Bell, P.M., and Virgo, D. (1980) High-pressure experiments on the iron
655 oxide wüstite ($Fe_{1-x}O$). Carnegie Institute of Washington Yearbook, 79, 374-376.
656

Figure captions

Fig. 1: Back scattered electron image of the polished run products of run MA-367 (a), run MA-380 (b) and run MA-376 (d). In Fig 1a the main grey-colored matrix represents majorite (Maj), the dark grey phase is stishovite (Sti), deep dark phase is magnesite (Mgs) and the light phase corresponds to the Fe-oxide. In Fig. 1b only majorite (grey), stishovite (dark grey) and an Fe-oxide phase (light light) are present. Fig. 1 c shows a combined element mapping image, i.e. phase map of run product MA-367: in yellow the main phase majorite, red the stishovite, blue the Fe-oxide and green the Fe-bearing magnesite. Fig. 1c is a slightly smaller portion of Fig. 1a and the black line is a guide for the eye and connects one and the same oxide grain in the two different images. Fig. 1 d is a representative BSE image of the Fe-oxide phase of run MA376.

Fig. 2: STEM image of a part of the FIB foil cut from an Fe-oxide grain of MA-367. The foil's dimensions are 15 × 10 × 0.150 μm. Two phases can be distinguished. The α-phase was identified as h-magnetite and the β-phase as goethite. The oriented intergrowth of the phases indicates that goethite is a secondary phase.

Fig. 3: Three dimensional ADT reconstructed diffraction volumes from the sample MA-367: (a) diffraction volume from α-phase viewed down a* (a) and down b* (b); (c) diffraction volume collected from an area containing both α-phase and β-phase viewed along different projections (c-d). The difference of α-phase and β-phase is evident due to the different length of c* vector and due to the A-centered pattern of α-phase. Both phases have related crystallographic orientations. Extinctions with rule $hkl : k + l = 2n$ are recognizable for the α-phase in panels a and c. We stress that these are projections of three-dimensional diffraction volumes, and the extinctions visible in panels a and c involve full columns of reflections along $h00$.

682 Fig. 4a, b: Selected area electron diffraction images of the mixed valence iron oxide indexed
683 on the basis of the structure proposal obtained in this study using ADT. With this figure we
684 prove that the iron oxide is h-magnetite.
685 Fig. 5: Observed, calculated (LeBail Fit) and difference X-ray powder pattern of the run
686 product MA-376 using the structural data of h-Fe_3O_4 (h-mgt) and stishovite (sti). Data were
687 collected in transmission using a STOE STADI P diffractometer (Cu$K\alpha_1$ radiation).
688 Convergence was achieved with R_{Bragg} *in %* = 1.7.
689 Fig. 6: Representative EEL spectra displaying the Fe $L_{2,3}$-edges of a majorite, synthesized by
690 Lenz et al. (2012) of similar composition than in this study at 18 GPa and 1500 °C and h-
691 Fe_3O_4 of run MA-367. The spectrum for iron oxide does not show the characteristic L_3
692 splitting as present for majoritic garnet. In addition the maxima of the L_3 and L_2 egdes are
693 shifted to lower energy compared to cubic magnetite, e.g. the maximum of the L_3 of
694 magnetite lies at 709 eV (van Aken and Liebscher 2002). Applying the calibration by van
695 Aken and Liebscher (2002) the averaged Fe^{3+}/Fe_{total} ratio was for both phases about 25% for
696 eight analyses which is much too low for either Fe_4O_5 or magnetite.
697 Fig. 7: Infrared spectra (a) of a single crystal majorite of run MA-380 showing the typical OH
698 bands for majorite, (b) of a multi-phase aggregate of run MA-380, (c) of a single crystal
699 majorite and (d) of a multi-crystal aggregate the later two taken from run MA-337 of Lenz et
700 al. (2012). The starting material of this run has a similar bulk composition but water in excess
701 (run conditions 18 GPa, 1500 °C, 3 hours). All spectra show the typical OH bands around
702 3100 and 3600 cm^{-1}. Spectra b and d (aggregates) show in addition a broad OH band around
703 3400 cm^{-1} resulting from vibrations of molecular water, most probably located on the grain
704 boundaries of the majorite aggregates. Compared to the majorite phase (c) of MA-337 which
705 contained 2200 ppm H_2O by weight majorite crystals of run MA-380 (a) contain about 1000
706 wt ppm H_2O. In the multi-phase aggregate of MA-380 no additional absorption feature than
707 those of OH in majorite can be observed. The thickness of the crystals was each 100 μm.

710 Table 1: Electron microprobe analyses and calculated cations pfu (n= number of
711 measurements; numbers in parenthesis are 1σ standard deviation on the last digits)

MA-367	h-Fe_3O_4	majorite	stishovite	carbonate*
	n = 13	n = 20	n = 4	n=3
FeO	72.07(14)	17.33(24)	0.70(16)	15.99
Cr_2O_3	10.21(4)	1.98(14)	0.15(6)	-
MgO	4.93(9)	19.86(19)	0.24(9)	36.10
Al_2O_3	4.89(5)	18.95(5)	1.81(8)	-
SiO_2	2.31(7)	43.11(17)	1.35(9)	-
Σ	94.41	101.26	100.54	52.09
	4 oxygens	12 oxygens	2 oxygens	3 oxygens
Fe^{2+}	0.75(1)	1.05(4)	0.01(1)	0.20
Fe^{3+}	1.39(1)	-	0.00(1)	-
Cr^{3+}	0.29(1)	0.11(3)	0.00(1)	-
Mg	0.26(1)	2.14(2)	0.00(1)	0.80
Al	0.21(1)	1.61(1)	0.02(1)	-
Si	0.08(1)	3.11(2)	0.98(1)	-
Σ	3.00	8.02	1.01	1

MA-376	h-Fe_3O_4	wadsleyite
	n = 12	n = 3
FeO	73.01(16)	0.19(7)
Cr_2O_3	12.16(6)	0.02(1)
MgO	0.02(9)	54.82(16)
Al_2O_3	5.45(8)	0.09(1)
SiO_2	1.35(9)	41.88(14)
Σ	91.99	97.00
	4 oxygen	4 oxygen
Fe^{2+}	1.02(1)	0.01(1)
Fe^{3+}	1.30(1)	-
Cr^{3+}	0.37(1)	0.00(1)
Mg	0.00(1)	1.97(2)
Al	0.25(1)	0.01(1)
Si	0.05(1)	1.01(1)
Σ	3.00	3.00

* carbon was calculated by stoichometry

712
713 Table 2: Extinction rules for space groups *Bbmm* and *Amam*. The "=*2n*" is omitted

Point group (*mmm*)	*hkl*	*0kl*	*h0l*	*hk0*	*h00*	*0k0*	*00l*
Bbmm	*h + l*	*k, l*	*h + l*	*h*	*h*	*k*	*l*
Amam	*k + l*	*k + l*	*h, l*	*k*	*h*	*k*	*l*

714
715
716

Table 3: Experimental details about ADT data sets and related ab-initio structure solutions and refinements.

	Crystal 1	**Crystal 2**
a (Å)	9.8(2)	
b (Å)	9.6(2)	
c (Å)	2.87(6)	
α (°)	90	
β (°)	90	
γ (°)	90	
Space group	*Amam*	
Wavelength of radiation (Å)	0.0197	0.0197
Max resolution (Å)	0.80	0.80
Unique reflections	121	171
Reflection completeness (%)	69	97
R_{int} (%)	17.77	20.32
Range of *h*, *k*, *l*	$-10 < h < 10$	$-12 < h < 12$
	$-12 < k < 12$	$-12 < k < 12$
	$-3 < l < 3$	$-3 < l < 3$
$R_{(SIR2011)}$	24.26	24.36
$R1_{(4\sigma)}$ (%)	33.11	38.33
$R1_{all}$ (%)	33.83	39.77
GooF	5.248	4.500
Least-squares parameters	16	16

Table 4: Ab-initio solution by direct methods (SIR2011) and structure refined by least squares (SHELX97) on the basis of ADT electron diffraction data. First column: atom name; second column: value of the maxima recognized in the potential map (the 1st ghost height is reported for comparison); third to fifth columns: fractional coordinates of the solution proposed ab-initio; sixth to eight columns: fractional coordinates refined by least squares; ninth column: partial occupancy Fe:Cr and Fe:Mg; tenth column: isotropic thermal factor U. Solution and refinement from "Crystal 1" data.

	Ab-initio solution – SIR2011					**Refinement – SHELX97**				
Atom name	**Height (e/Å^3)**	**Multipl.**	**x**	**y**	**z**	**x**	**y**	**z**	**Fe : Cr Fe : Mg**	**U(iso) (Å^2)**
Fe1	3.59	8	0.423	0.630	1	0.431	0.633	1	3.3 : 1	0.005
Fe2	3.54	4	¼	0.388	½	¼	0.376	½	1.5 : 1	0.012
O1	1.70	4	½	½	½	½	½	½		0.032
O2	1.60	4	¼	0.537	1	¼	0.540	1		0.104
O3	1.46	8	0.393	0.266	1	0.378	0.275	1		0.022
1st ghost	0.67									

735 Table 5: Transmission electron microscopic analyses; numbers in parentheses behind the
736 experimental data are 1σ standard deviation on the last digits
737
738

MA-367			
exp	h-Fe_3O_4	exp	h-Fe_3O_4
4.220(9)	4.294 (120)	47.08(5)°	47.0° (131)/(120)
2.716(9)	2.749 (011)	27.95(5)°	28.5° (131)/(011)
2.053(9)	2.084 (131		
MA-376			
exp	h-Fe_3O_4	exp	h-Fe_3O_4
9.948(6)	9.990 (100)	26.05(6)°	25.62° (1209/(010)
4.738(6)	4.790 (020)	63.95(6)°	64.38° (120)/(100)
4.291(6)	4.319 (120)		

739 The calculated *d*-spacings of h-Fe_3O_4 are based on the structural proposal and the lattice parameter (Å) derived
740 in this study: *a* 9.8 *b* 9.6 *c* 2.87 for MA-367 and *a* 9.9 *b* 9.58 *c* 2.83 for MA-376.
741

742

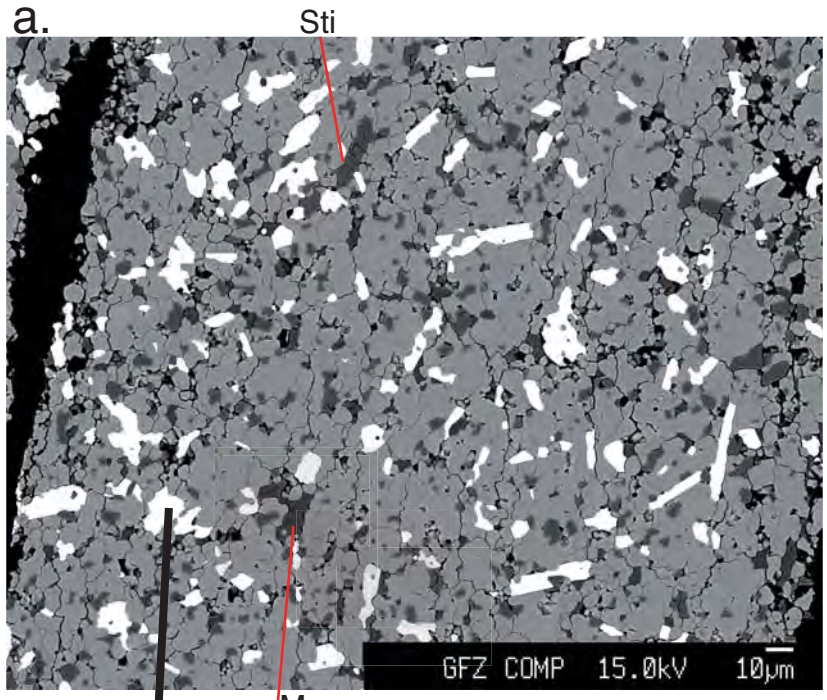

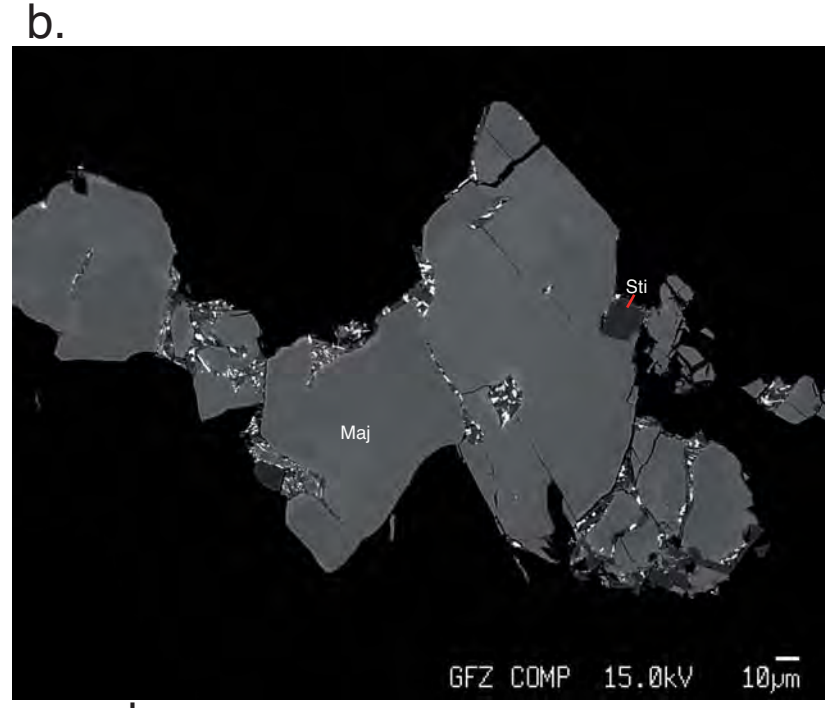

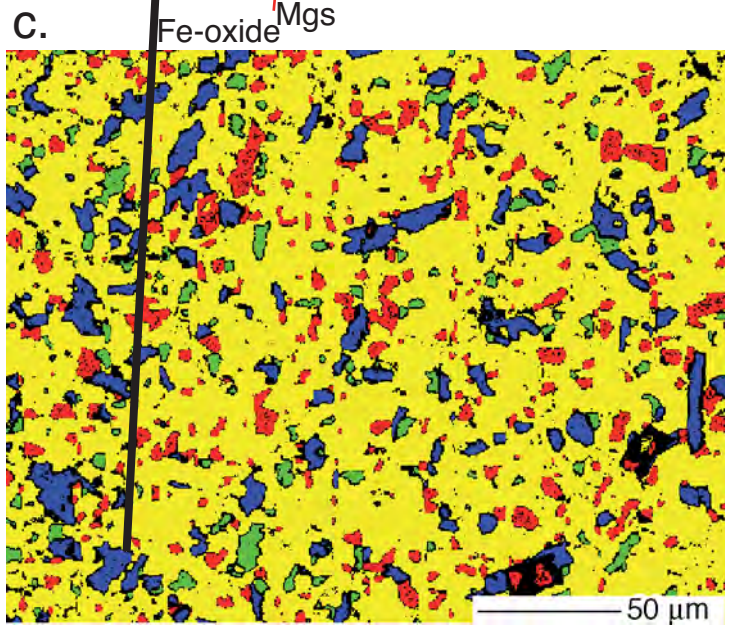

yellow Maj
red Sti
blue Fe-oxide
green Magnesite

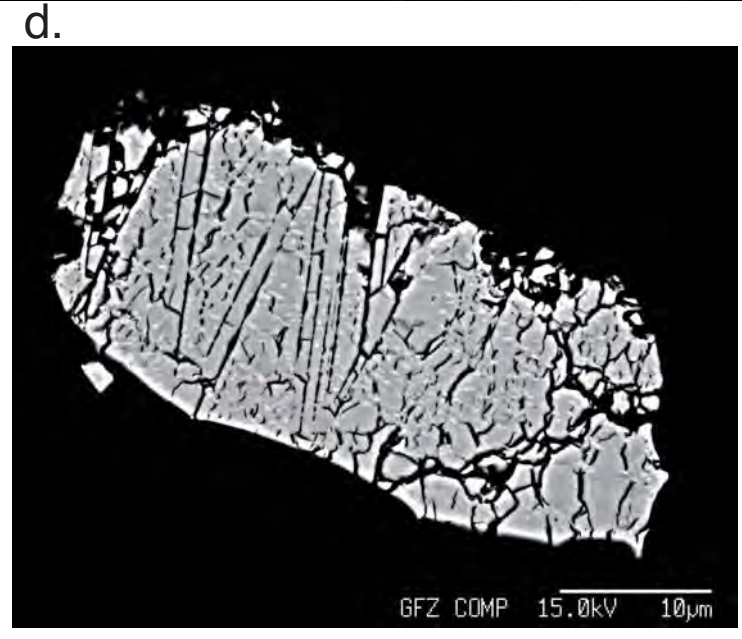

Fig.1

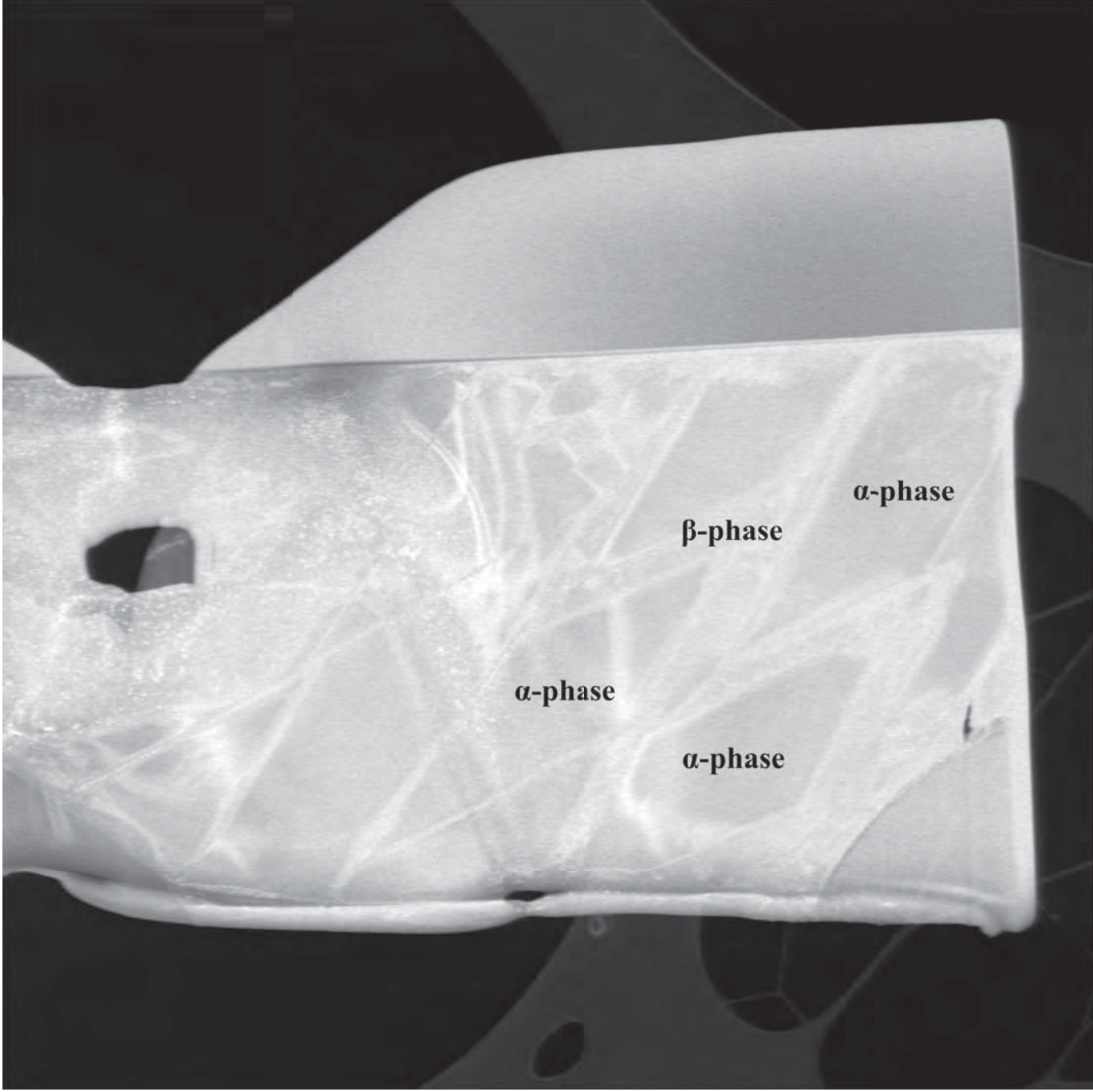

Fig. 2

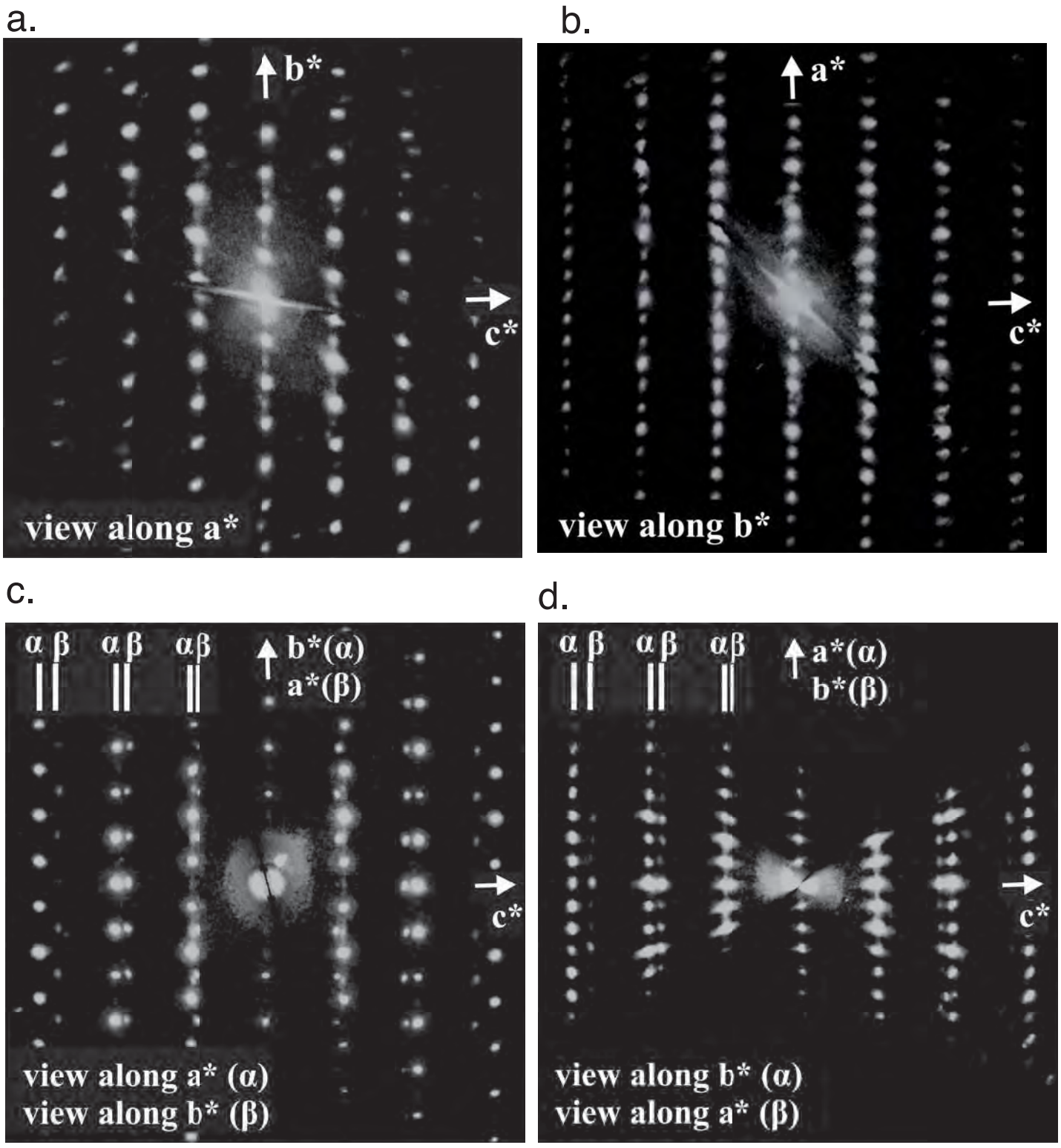
a.
b*
c*
view along a*
b.
a*
c*
view along b*
c.
α β
α β
αβ
b*(α)
a*(β)
c*
view along a* (α)
view along b* (β)
d.
α β
α β
αβ
a*(α)
b*(β)
c*
view along b* (α)
view along a* (β)

Fig. 3 a-d

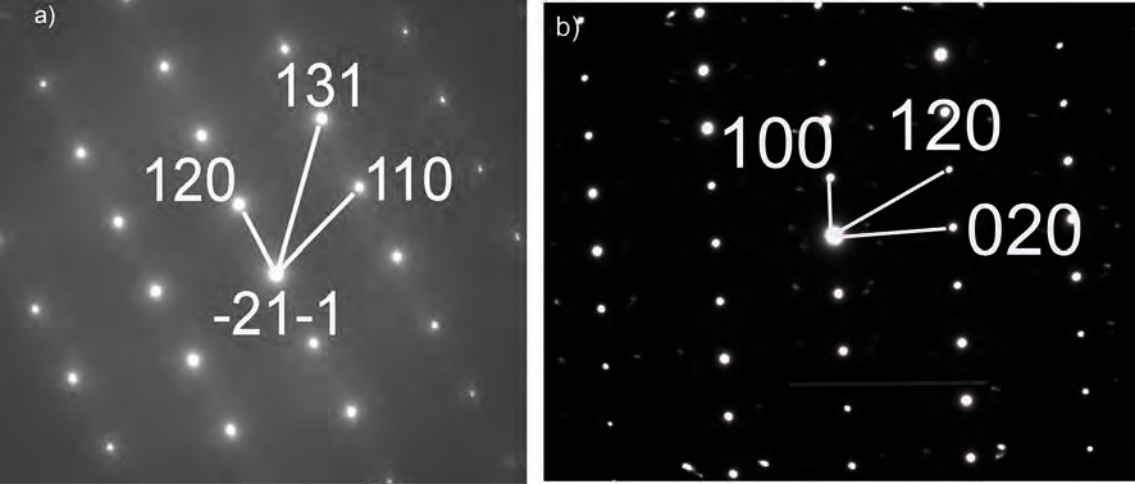
a)
131
120
110
-21-1
b)
100
120
020

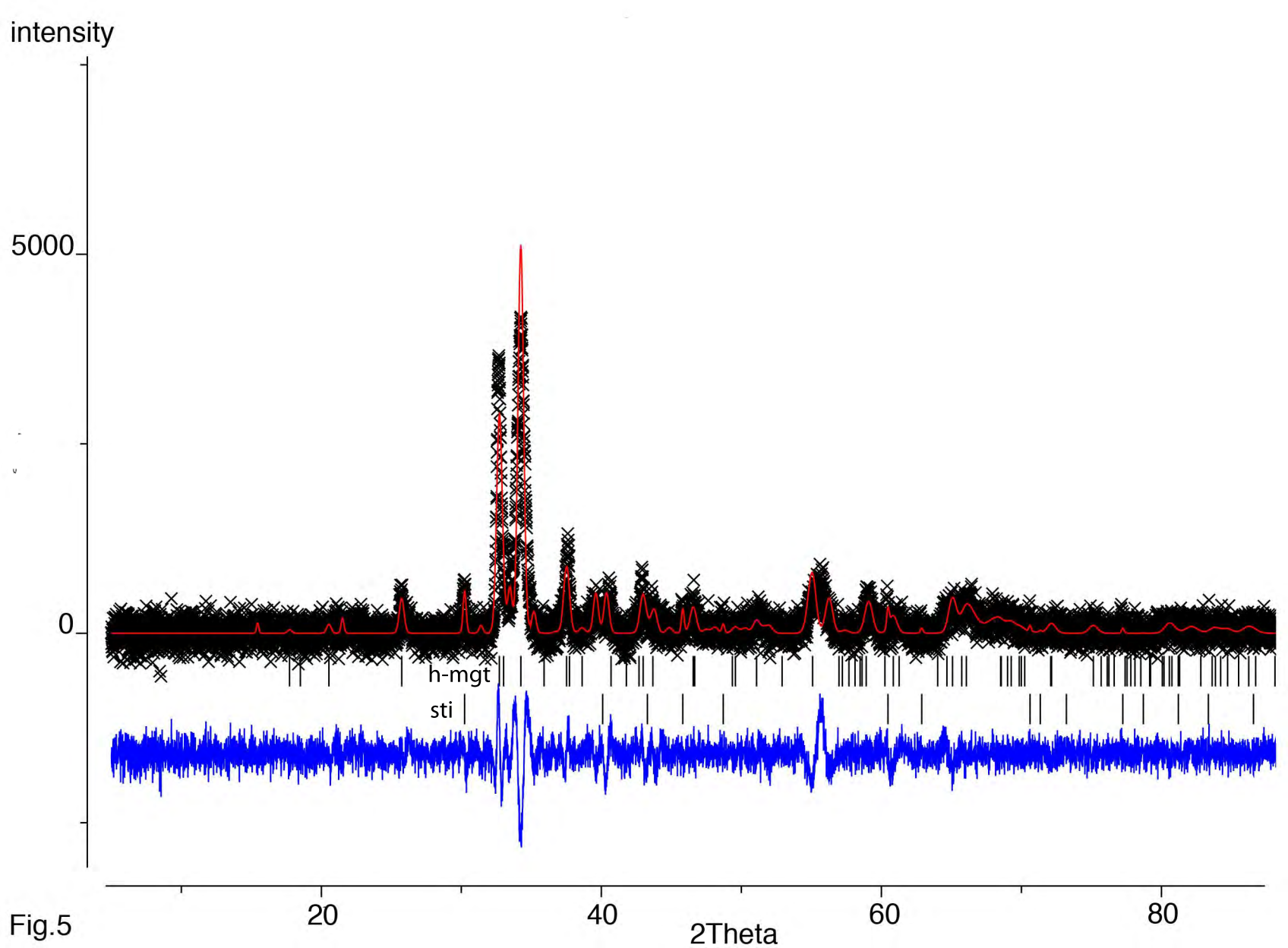

Fig.5

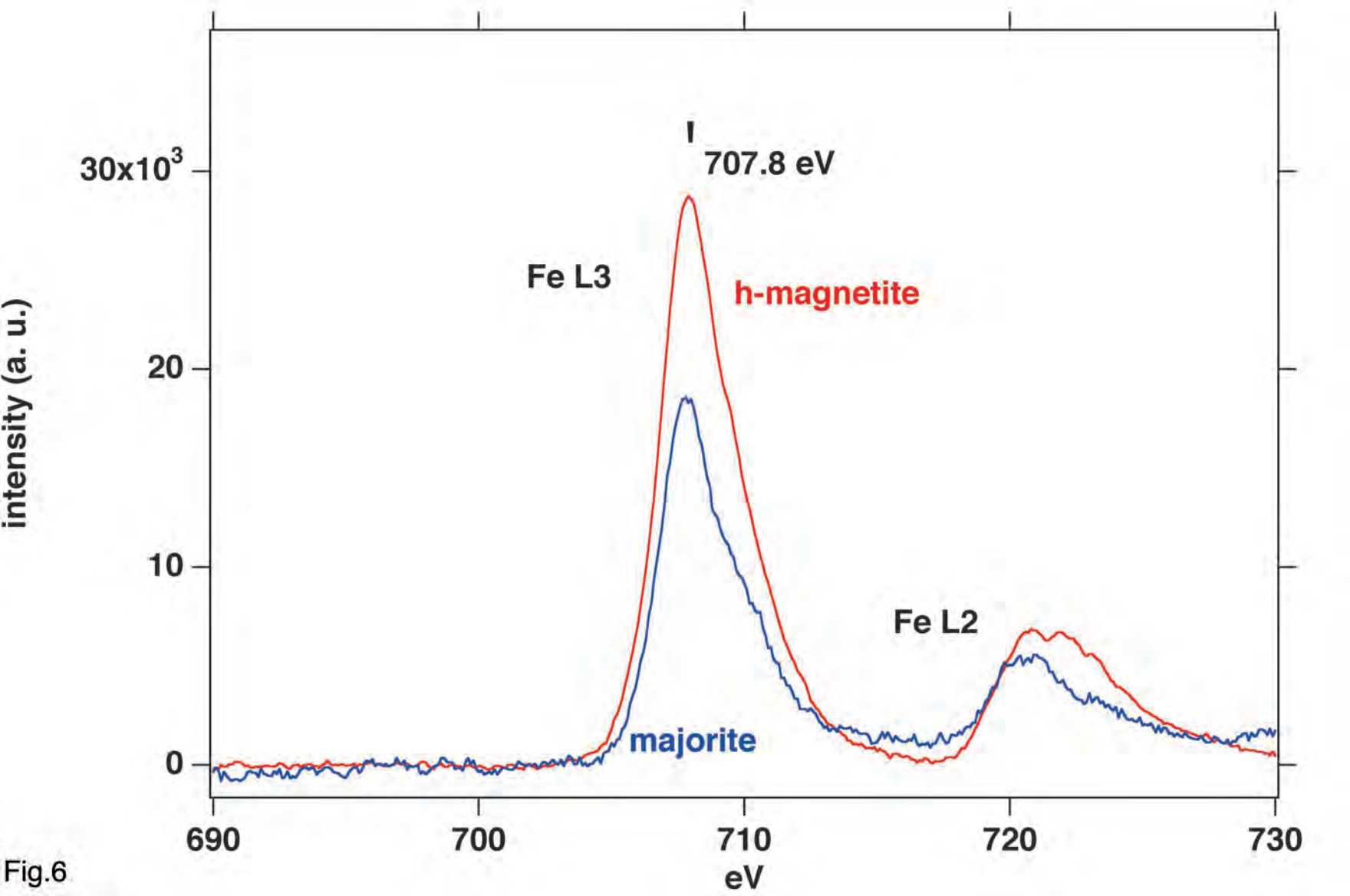
30x10^3
20
10
0
intensity (a. u.)
707.8 eV
Fe L3
h-magnetite
Fe L2
majorite
690
700
710
720
730
eV

Fig.6

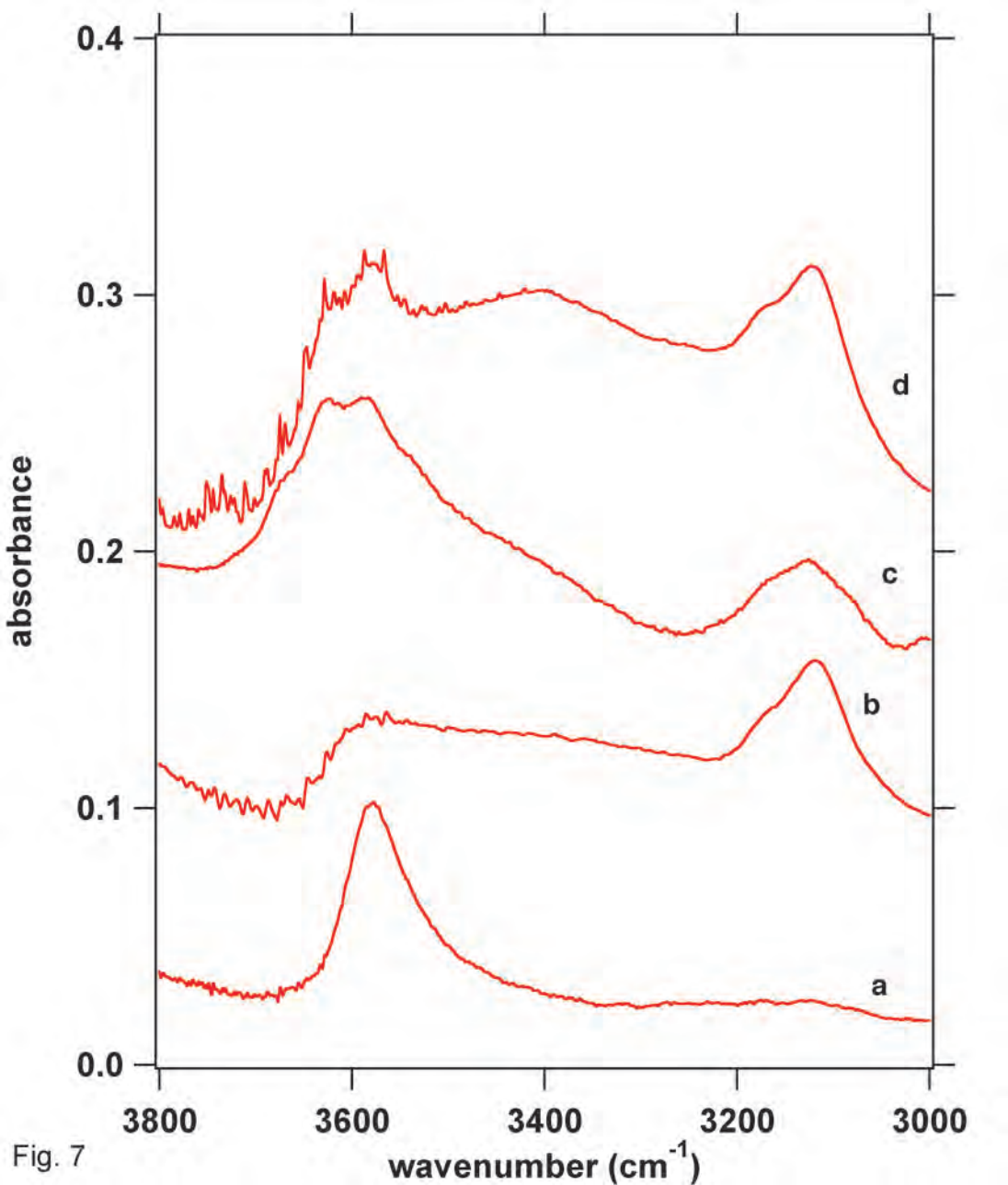
0.4
0.3
0.2
0.1
0.0
absorbance
d
c
b
a
3800
3600
3400
3200
3000
wavenumber (cm-1)

Fig. 7